

Compressively strained Triple-layer $\text{IrO}_6/\text{MnO}_6$ Octahedral Nanosheets for Oxygen Evolution in Acid Media

Wenli zhao

Central South University

Fenghua Xu

Central South University

Zhipeng Pan

Guizhou Meling Power Sources Co., Ltd

Min Liu

Central South University

Baicheng Weng (✉ bcweng@mail.csu.edu.cn)

Central South University

Article

Keywords: Compressive strain, Oxygen evolution reaction, Nanosheets, Acid, Iridium

Posted Date: May 12th, 2022

DOI: <https://doi.org/10.21203/rs.3.rs-1531422/v1>

License:   This work is licensed under a Creative Commons Attribution 4.0 International License.

[Read Full License](#)

Abstract

Oxygen electrochemistry plays a key role in renewable energy technologies such as fuel cells and electrolyzers, but its slow kinetics limits the performance and commercialization of such devices. Here, a novel triple-layer IrO₆/MnO₆ nanosheet was developed by a simple hydrothermal method. During the substitution of Mn by Ir, lattice compressive strain is introduced into the IrO₆/MnO₆ nanosheets, thereby tuning their electronic structure to suit the favorite oxygen evolution reaction (OER) activity. This compressively strained nanosheet catalyst exhibits an excellent mass activity of 7882 A g⁻¹ at an overpotential of 270 mV in 0.5 M H₂SO₄, and reaches 10, 50 and 100 mA cm⁻² at overpotentials of only 62 mV, 197 mV and 234 mV, respectively, ranking the highest OER activity among the state-of-the-art values in acid media. The catalyst exhibits a remarkable stability even at 300 mA cm⁻² in 0.5 M H₂SO₄. Using the nanosheets as OER catalyst and NiMo alloy as hydrogen evolution reaction catalyst, a two-electrode electrolyzer achieves 10 mA cm⁻² with only a cell voltage of 1.46 V for overall water splitting in 0.5 M H₂SO₄. This strategy enables the material with high feasibility for practical applications on hydrogen production.

Introduction

Electrochemical water splitting to produce clean and recyclable hydrogen fuels provides a desirable solution to solve the current energy shortage and environmental pollution issues¹⁻³. Water splitting involves oxygen evolution reaction (OER) and hydrogen evolution reaction (HER). OER is significantly more challenging than HER, because OER involves multiple electron transfer and is kinetically sluggish⁴⁻⁷. Compared with alkaline electrolysis, oxygen production in acid media has the advantages of simplicity, high-current density, and high-pressure compatibility⁸⁻¹⁰. At present, high-performance catalysts for OER in acid media are mostly limited to noble metal oxides, such as IrO₂¹¹. However, their scarcity, low mass activities and large overpotentials at high current densities limit the economically large-scale electrochemical water splitting.

These difficulties mainly arise from tuning the electronic structure of IrO_x in stable Ir-based oxides and exposing them efficiently to electrolytes with lower Ir content. For instance, 6H-SrIrO₃ exhibited a high OER activity under acidic conditions due to the presence of IrO₆ octahedra, which were proved to be the active sites for OER¹². However, in order to maintain the stable 6H-SrIrO₃ perovskite structure, a large amount of electrochemically inactive bulk SrO₆ octahedra is required. As a result, it would be very difficult to reduce the Ir content while avoiding the instability of structure. Seitz et al. propose an efficient method to expose active sites and tune electronic structures via Sr leaching on SrIrO₃ surfaces¹³. The electronic structure adjustment is validated through the increased valence state of Ir. Although the high valence stated IrO_x on the surface accounts for the high activities, the low activity of the inner substrate reduces the overall mass activity. Therefore, fully exposing IrO₆ octahedra and tuning its electronic structure would be greatly beneficial for OER activity. Strain is proved to be an effective way to enhance the OER activity by

distorting the crystal structure to tailor the electronic structures. For instance, torsion strain through grain boundary engineering and atomic replacement synergistically tuned the adsorption energy of oxygen intermediates and boosted the OER activity¹⁴. Therefore, few layers of strained IrO₆ octahedra would be ideal catalysts for realizing fully exposed IrO₆ octahedra and modified the electronic structure for efficient and stable OER.

In this study, we adopted a facile hydrothermal approach to fabricate a new layered Mn_{1-x}Ir_xO₂ nanosheet electrocatalyst with compressively strained IrO₆/MnO₆ octahedra (*s*-Mn_{1-x}Ir_xO₂). The obtained *s*-Mn_{0.98}Ir_{0.02}O₂ catalyst exhibits the highest iridium mass activity (7882 A g⁻¹ at an overpotential of 270 mV) and only needs an ultra-low overpotential of 62 mV to achieve a current density of 10 mA cm⁻². More notably, a two-electrode electrolyzer with *s*-Mn_{0.98}Ir_{0.02}O₂ as the OER catalyst and NiMo alloy as the HER catalyst for overall water splitting in 0.5 M H₂SO₄ reaches a current density of 10 mA cm⁻² at a cell voltage of only 1.46 V and shows excellent stability.

Results And Discussion

For an OER process, the binding strength of three reaction intermediates (OH*, O* and OOH*) to active sites determines the energetics¹⁵⁻¹⁷. $\Delta G_{O^*} - \Delta G_{OH^*}$ and ΔG_{OOH^*} are used as appropriate descriptors for OER activity^{16,18,19}. We developed a new layered catalyst by inserting trace Ir to δ -MnO₂ and meanwhile introducing lattice compressive strain, which was defined as *s*-Mn_{1-x}Ir_xO₂ (**Supplementary Table 1**). All the calculated structural models are indicated in Fig. 1a. Figure 1b shows a constructed contour plot based on the calculated results. It is found that bulk MnO₂ with corner-shared octahedra has a high ΔG_{OOH^*} , meaning a low binding energy. With the formation of layered structure (δ -MnO₂), ΔG_{OOH^*} decreases, and $\Delta G_{O^*} - \Delta G_{OH^*}$ increases, leading to both descriptors moving towards the ideal zone. The layered Mn_{1-x}Ir_xO₂ (*l*-Mn_{1-x}Ir_xO₂) gives a theoretically lower overpotential of 230 mV, due to the slightly increased OOH* absorption energy on electronic structure modulated IrO_x in *l*-Mn_{1-x}Ir_xO₂. With the introduction of lattice compressive strain into *l*-Mn_{1-x}Ir_xO₂, the obtained *s*-Mn_{1-x}Ir_xO₂ exhibits appropriate $\Delta G_{O^*} - \Delta G_{OH^*}$ and ΔG_{OOH^*} , and a lowest overpotential of 150 mV. Remarkably, the free energy of ΔG_2 (**Supplementary Table 1**) for *s*-Mn_{1-x}Ir_xO₂ is 1.22 eV, which is very close to the theoretical value of 1.23 eV, indicating an optimized electronic structure under lattice compressive strain. Continuous projected density of states (PDOS) (**Supplementary Fig. 1**) indicates that *d* (ρ_d) and *p* (ρ_p) band centers in *s*-Mn_{1-x}Ir_xO₂ moves closer to Fermi level and O 2*p* compared to *l*-Mn_{1-x}Ir_xO₂ without strain. Further theoretical electronic structure analysis reveals that lattice compressive strain reduces the catalytic energy barriers, facilitates the electron transfer, and thereby favors the enhancement in OER activity.

To experimentally validate the calculated results, the compressively strained Mn_{1-x}Ir_xO₂ ultra-thin nanosheets (*s*-Mn_{1-x}Ir_xO₂) were synthesized through a simple one-step hydrothermal reduction method

(Scheme 1, Supporting Information). XRD patterns of $s\text{-Mn}_{1-x}\text{Ir}_x\text{O}_2$ (Fig. 2a and Supplementary Fig. 2a) show the identical peak positions as those of $\delta\text{-MnO}_2$, suggesting it strongly (001) facet oriented.

Scanning electron microscope (SEM) images of $s\text{-Mn}_{1-x}\text{Ir}_x\text{O}_2$ show nanosheets arranged vertically on the surface of carbon paper (Fig. 2c and Supplementary Fig. 2b). Transmission electron microscope (TEM) measurement (Fig. 2d) of $s\text{-Mn}_{0.98}\text{Ir}_{0.02}\text{O}_2$ shows a curved nanosheet morphology. The sharp decrease of the contact angle (θ) value (Supplementary Fig. 3) indicates that the obtained $s\text{-Mn}_{1-x}\text{Ir}_x\text{O}_2$ sample is beneficial to the rapid mass diffusion of electrolyte on the catalyst surface^{20,21}. The thickness of the nanosheets determined by atomic force microscopy (AFM) is about 4–4.5 nm (Fig. 2e), corresponding to only three monolayers of $\text{IrO}_6/\text{MnO}_6$ octahedral dimers. The ultra-thin nanosheet morphology enables full exposure active sites of $\text{IrO}_6/\text{MnO}_6$ ^{22,23}. The analyses of elemental composition (Supplementary Tables 2 and 3, Supplementary Fig. 4) reveal that Mn, Ir and O elements uniformly disperse in the synthesized nanosheets without any aggregation.

Aberration corrected high-angle annular dark-field scanning transmission electron microscope (HAADF-STEM) was used to characterize the lattice compressive strain. For comparison, a strain-free sample ($t\text{-Mn}_{0.98}\text{Ir}_{0.02}\text{O}_2$) was synthesized by annealing the $s\text{-Mn}_{0.98}\text{Ir}_{0.02}\text{O}_2$ sample from room temperature to 400 °C at 1.0 °C min⁻¹ to eliminate the strain. Figures 2f and 2g show clear lattice fringes for $t\text{-Mn}_{0.98}\text{Ir}_{0.02}\text{O}_2$ and $s\text{-Mn}_{0.98}\text{Ir}_{0.02}\text{O}_2$, respectively, indicating a single crystal structure without phase separation. For the annealed sample, $t\text{-Mn}_{0.98}\text{Ir}_{0.02}\text{O}_2$, the integrated pixel intensity indicates that the O-O lattice spacing is 0.244 nm (Fig. 2h), which is consistent with that of $\delta\text{-MnO}_2$ ²⁴ and suggests no compressive strain in it. Given that the bond angle of metal-O-metal is around 100° in a typical MnO_6 octahedron, the metal-O bond length for $t\text{-Mn}_{0.98}\text{Ir}_{0.02}\text{O}_2$ is about 0.198 nm. However, for $s\text{-Mn}_{0.98}\text{Ir}_{0.02}\text{O}_2$, the O-O lattice spacing shrinks to 0.228 nm (Fig. 2i), and the Mn/Ir-O bond length is shortened to about 0.183 nm. Combining the IrO_6 octahedral unit cell is larger than that of the MnO_6 octahedral, it can be concluded that the incorporation of trace amount of Ir into Mn-O lattice induces lattice compressive strain.

The electronic structures were further explored by X-ray absorption near-edge structure (XANES) and extended X-ray absorption fine structure (EXAFS) measurements. Wavelet transform of EXAFS (WT-EXAFS) (Fig. 3a, b) of Ir L₃-edge related to Ir–O bond for $s\text{-Mn}_{0.98}\text{Ir}_{0.02}\text{O}_2$ shows an increased intensity of 6.0 at 5.0 Å⁻¹ compared to 3.0 for IrO_2 , demonstrating higher valence states of Ir in $s\text{-Mn}_{0.98}\text{Ir}_{0.02}\text{O}_2$. The higher valence states of Ir in $s\text{-Mn}_{0.98}\text{Ir}_{0.02}\text{O}_2$ is further verified by higher intensity of Ir L₃-edge white line of $s\text{-Mn}_{0.98}\text{Ir}_{0.02}\text{O}_2$ than that of IrO_2 (Fig. 3c)^{25–27}. The fitting results for Fourier transform of EXAFS (FT-EXAFS) spectra (Fig. 3d) exhibit that Ir-O bond in $s\text{-Mn}_{0.98}\text{Ir}_{0.02}\text{O}_2$ is covalently contracted to 1.96 Å from 1.99 Å of IrO_2 (Supplementary Table 4), leading to 1.51% compressive strain. This result is also evidenced by X-ray photoelectron spectroscopy (XPS) analysis. As shown in Fig. 3g, the peak positions corresponding to Ir 4f_{7/2} and Ir 4f_{5/2} in $s\text{-Mn}_{0.98}\text{Ir}_{0.02}\text{O}_2$ move to higher binding energies by 0.20 eV

compared to those of IrO₂^{25,28}. High valence state and electrophilic Ir favors water molecule attack for promoting the formation of O-O bonds during OER catalysis²⁹⁻³².

Mn K-edge XANES spectrum of *s*-Mn_{0.98}Ir_{0.02}O₂ (Fig. 3e) is quite different from that of δ -MnO₂, implying a varied coordination environment of Mn in *s*-Mn_{0.98}Ir_{0.02}O₂. The absorption energy of *s*-Mn_{0.98}Ir_{0.02}O₂ between 6540 and 6560 eV shifts slightly to lower energy than that of δ -MnO₂, indicating that the average valence state of Mn in *s*-Mn_{0.98}Ir_{0.02}O₂ is less than 4⁺³³⁻³⁵. FT-EXAFS spectra (Fig. 3f) display *s*-Mn_{0.98}Ir_{0.02}O₂ have 3 identical characteristic peaks from 1.0 to 3.5 Å as δ -MnO₂, assigned to Mn-O (~ 1.50 Å), Mn-Mn edge-sharing (~ 2.5 Å) and Mn-Mn corner-sharing (~ 3.0 Å) scattering shells, respectively. However, further fitting analysis (**Supplementary Table 4**) shows that Mn - Mn edge-sharing bond length of *s*-Mn_{0.98}Ir_{0.02}O₂ shrinks to 2.86 Å from 2.89 Å of δ -MnO₂, resulting in .03 % lattice compressive strain.

The OER electrochemical performance of the compressively strained *s*-Mn_{0.98}Ir_{0.02}O₂ was measured using a proton exchange membrane separated electrochemical cell with Pt plate as the counter electrode and Hg/Hg₂SO₄ as the reference electrode. IrO₂ and δ -MnO₂ were utilized for comparison. The current densities of *s*-Mn_{1-x}Ir_xO₂ (*x* = 0.01, 0.02) are more than a dozen orders of magnitude higher than that of IrO₂ and MnO₂ at the same voltage (Fig. 4a). Especially, *s*-Mn_{1-0.98}Ir_{0.02}O₂ can reach a current density of 176.2 mA cm⁻² at an overpotential of 270 mV, while IrO₂ and δ -MnO₂ only can achieve 4.0 and 0.2 mA cm⁻², respectively, at the same bias. *s*-Mn_{0.98}Ir_{0.02}O₂ with the lowest Tafel slope of 18.1 mV dec⁻¹ (Fig. 4b) exhibits the best OER kinetics³⁶.

In contrast, *t*-Mn_{1-x}Ir_xO₂ without strain shows inferior OER activity to *s*-Mn_{1-x}Ir_xO₂, although it still has much higher OER activity than IrO₂. In particular, the OER activity of *s*-Mn_{0.98}Ir_{0.02}O₂ is 1.6 times higher than that of *t*-Mn_{0.98}Ir_{0.02}O₂ at an overpotential of 270 mV. Meanwhile, the overpotentials for *s*-Mn_{0.98}Ir_{0.02}O₂ to reach 10, 50 and 100 mA cm⁻² are 62, 197 and 234 mV, respectively, much lower than those for *t*-Mn_{0.98}Ir_{0.02}O₂ (105, 227 and 266 mV, respectively) (Fig. 4d). These results demonstrate that the compressive strain has a positive effect on OER activity.

The charge transfer was further analyzed by electrochemical impedance spectroscopy (EIS). Nyquist plots (Fig. 4c) reveal that *s*-Mn_{0.98}Ir_{0.02}O₂ have smaller charge transfer resistance (R_{ct} = 1.954 Ω) compared to *t*-Mn_{0.98}Ir_{0.02}O₂, δ -MnO₂, IrO₂, suggesting that the integration of compressive strain accelerates charge transfer. The compressive strain can push the *d*/*p* band centers closer to the Fermi level. As a result, the holes in the O 2*p* orbitals will more easily transfer to the catalyst surface to facilitate the charge transfer, resulting in the improvement of OER activity. Remarkably, *s*-Mn_{0.98}Ir_{0.02}O₂ exhibits the highest OER activity at the lower Ir loading amount among the state-of-the-art electrocatalysts (Fig. 4e, **Supplementary Table 5**).

Next, we evaluate the mass activity of Ir, which refers to the current per unit mass of Ir and is an important aspect for the catalytic performance of acidic OER electrocatalysts. At 270 mV, the mass activity of IrO₂ is

only 9 A g^{-1} , while that of $s\text{-Mn}_{0.98}\text{Ir}_{0.02}\text{O}_2$ is up to 7882 A g^{-1} , outperforming the state-of-the-art OER electrocatalysts (Fig. 4f) ^{37–43}.

The stability of $s\text{-Mn}_{0.98}\text{Ir}_{0.02}\text{O}_2$ was evaluated in acidic condition with the current density of 10 mA cm^{-2} with IrO_2 and $\delta\text{-MnO}_2$ for comparison (Fig. 4g). No attenuation of the electrocatalytic activity is observed after the $s\text{-Mn}_{0.98}\text{Ir}_{0.02}\text{O}_2$ catalyst runs for 48 h. In contrast, the OER activity of IrO_2 declines obviously even after 32 h. Then we continue to run this catalyst at a high current density of 100 mA cm^{-2} for another 48 h, and at a higher current density of 300 mA cm^{-2} for extra 72 h. Remarkably, this catalyst can still maintain over 95% activity after more than 168 h (7 days) durability test, indicating excellent stability.

In view of excellent OER activity of $s\text{-Mn}_{0.98}\text{Ir}_{0.02}\text{O}_2$ in this work and high HER activity of NiMo alloy in the previous work^{44–46}, a two-electrode system with $s\text{-Mn}_{0.98}\text{Ir}_{0.02}\text{O}_2$ as the anode and NiMo alloy as the cathode ($s\text{-Mn}_{0.98}\text{Ir}_{0.02}\text{O}_2 \parallel \text{NiMo}$) was assembled for overall water splitting in $0.5 \text{ M H}_2\text{SO}_4$ with a scan rate of 5 mV s^{-1} . IrO_2 and NiMo alloy electrolytic cell ($\text{IrO}_2 \parallel \text{NiMo}$) was also evaluated for comparison. As expected, $s\text{-Mn}_{0.98}\text{Ir}_{0.02}\text{O}_2 \parallel \text{NiMo}$ electrolyzer only needs 1.46 V to reach a current density of 10 mA cm^{-2} (Fig. 5a, inset: optical photo of two-electrode electrolyzer), much lower than $\text{IrO}_2 \parallel \text{NiMo}$ (1.57 V), suggesting outstanding water splitting catalytic activity of the $s\text{-Mn}_{0.98}\text{Ir}_{0.02}\text{O}_2 \parallel \text{NiMo}$ electrolyzer. Furthermore, the $s\text{-Mn}_{0.98}\text{Ir}_{0.02}\text{O}_2 \parallel \text{NiMo}$ electrolytic cell is very stable for the overall water splitting in $0.5 \text{ M H}_2\text{SO}_4$ (Fig. 5b). However, $\text{IrO}_2 \parallel \text{NiMo}$ fluctuates evidently. Notably, the performance of the $s\text{-Mn}_{0.98}\text{Ir}_{0.02}\text{O}_2 \parallel \text{NiMo}$ system is superior to the current series of representative water splitting catalysts (**Supplementary Table 6**), which makes it the most active water splitting catalyst under acidic conditions.

Conclusions

We developed a compressively strained electrocatalyst, $s\text{-Mn}_{1-x}\text{Ir}_x\text{O}_2$ ultra-thin nanosheets, for OER in acid media through a simple hydrothermal method. Especially, $s\text{-Mn}_{0.98}\text{Ir}_{0.02}\text{O}_2$ exhibits excellent performance for OER with a small Tafel slope of 18.1 mV dec^{-1} , a high mass activity with 7882 A g^{-1} at an overpotential of 270 mV , low overpotential of 62 and 234 mV under the benchmark current density of 10 and 100 mA cm^{-2} , respectively. The fabricated catalyst also exhibits good stability even at high current density of 300 mA cm^{-2} for practical application, which is superior to currently reported catalysts. The remarkable performance is ascribed to the full exposure of compressively strained $\text{IrO}_6/\text{MnO}_6$ octahedral dimers. Moreover, when $s\text{-Mn}_{0.98}\text{Ir}_{0.02}\text{O}_2$ is used as OER catalyst, and NiMo alloy is used as HER catalyst for two-electrode overall water splitting, the cell shows high electrocatalytic activity, which can reach 10 mA cm^{-2} at 1.46 V .

Declarations

Acknowledgements

This work was financially supported by NSF project (No. 51202281, 21872174, and U1932148). The work was also partially supported by Hunan Key Technology R&D Program (2022GK2045, 2020WK2002), International Science and Technology Cooperation Program (Grant Nos. 2017YFE0127800 and 2018YFE0203400), Hunan Provincial Natural Science Foundation of China (No. 2020JJ2041), Changsha Municipal National Science Foundation (kq2014120) and the foundation of Hunan Environmental Protection Department. The authors also acknowledge the support from the High-Performance Computing Center of Central South University.

References

1. Yu, Z. Y. *et al.* Clean and affordable hydrogen fuel from alkaline water splitting: past, recent progress, and future prospects. *Adv. Mater.* **33**, 2007100 (2021).
2. McHugh, P. J., Stergiou, A. D. & Symes, M. D. Decoupled electrochemical water splitting: from fundamentals to applications. *Adv. Energy Mater.* **10**, 2002453 (2020).
3. Seh, Z. W. *et al.* Combining theory and experiment in electrocatalysis: insights into materials design. *Science* **355**, 146 (2017).
4. Koper, M. T. M. Thermodynamic theory of multi-electron transfer reactions: implications for electrocatalysis. *J. Electroanal. Chem.* **660**, 254–260 (2011).
5. Yao, Y. *et al.* Engineering the electronic structure of single atom Ru sites via compressive strain boosts acidic water oxidation electrocatalysis. *Nat. Catal.* **2**, 304–313 (2019).
6. Wang, M., Wang, Y., Mao, S. S. & Shen, S. Transition-metal alloy electrocatalysts with active sites modulated by metal-carbide heterophases for efficient oxygen evolution. *Nano Energy* **88**, 106216 (2021).
7. Blasco-Ahicart, M., Soriano-Lopez, J., Carbo, J. J., Poblet, J. M. & Galan-Mascaros, J. R. Polyoxometalate electrocatalysts based on earth-abundant metals for efficient water oxidation in acidic media. *Nat. Chem.* **10**, 24–30 (2018).
8. Khouya, A. Hydrogen production costs of a polymer electrolyte membrane electrolysis powered by a renewable hybrid system. *Int. J. Hydrog. Energy* **46**, 14005–14023 (2021).
9. Chatterjee, S. *et al.* Nanoporous iridium nanosheets for polymer electrolyte membrane electrolysis. *Adv. Energy Mater.* **11**, 2101438 (2021).
10. Reier, T., Nong, H. N., Teschner, D., Schlögl, R. & Strasser, P. Electrocatalytic oxygen evolution reaction in acidic environments - reaction mechanisms and catalysts. *Adv. Energy Mater.* **7**, 1601275 (2017).
11. Lim, J. *et al.* Ultrathin IrO₂ nanoneedles for electrochemical water oxidation. *Adv. Funct. Mater.* **28**, 1704796 (2018).
12. Yang, L. *et al.* Efficient oxygen evolution electrocatalysis in acid by a perovskite with face-sharing IrO₆ octahedral dimers. *Nat. Commun.* **9**, 5236 (2018).
13. Seitz, L. C. *et al.* A highly active and stable IrO_x/SrIrO₃ catalyst for the oxygen evolution reaction. *Science* **353**, 1011–1014 (2016).

14. Hao, S. *et al.* Torsion strained iridium oxide for efficient acidic water oxidation in proton exchange membrane electrolyzers. *Nat. Nanotechnol.* **16**, 1371–1377 (2021).
15. Calle-Vallejo, F. *et al.* Number of outer electrons as descriptor for adsorption processes on transition metals and their oxides. *Chem. Sci.* **4**, 1245–1249 (2013).
16. Man, I. C. *et al.* Universality in oxygen evolution electrocatalysis on oxide surfaces. *Chem.Cat.Chem.* **3**, 1159–1165 (2011).
17. Medford, A. J. *et al.* From the sabatier principle to a predictive theory of transition-metal heterogeneous catalysis. *J. Catal.* **328**, 36–42 (2015).
18. Bajdich, M., Garcia-Mota, M., Vojvodic, A., Norskov, J. K. & Bell, A. T. Theoretical investigation of the activity of cobalt oxides for the electrochemical oxidation of water. *J. Am. Chem. Soc.* **135**, 13521–13530 (2013).
19. Suen, N. T. *et al.* Electrocatalysis for the oxygen evolution reaction: recent development and future perspectives. *Chem. Soc. Rev.* **46**, 337–365 (2017).
20. Chen, Y. *et al.* Electrochemically inert g-C₃N₄ promotes water oxidation catalysis. *Adv. Funct. Mater.* **28**, 1705583 (2017).
21. Sun, Y. *et al.* Fe₃C/CoFe₂O₄ nanoparticles wrapped in one-dimensional MIL-53(Fe)-derived carbon nanofibers as efficient dual-function oxygen catalysts. *Chem. Eng.J.* **424** (2021).
22. Voiry, D. *et al.* Enhanced catalytic activity in strained chemically exfoliated WS₂ nanosheets for hydrogen evolution. *Nat. Mater.* **12**, 850–855 (2013).
23. Huang, J. *et al.* CoOOH nanosheets with high mass activity for water oxidation. *Angew. Chem., Int. Ed. Engl.* **54**, 8722–8727 (2015).
24. Liu, P. *et al.* Facile preparation of ultrafine manganese dioxide nanowires on activated carbon paper with enhanced capacitance for supercapacitors. *Ionics* **23**, 247–251 (2016).
25. Chen, Y. *et al.* Exceptionally active iridium evolved from a pseudo-cubic perovskite for oxygen evolution in acid. *Nat. Commun.* **10**, 572 (2019).
26. Zhang, Z. *et al.* Electrochemical deposition as a universal route for fabricating single-atom catalysts. *Nat. Commun.* **11**, 1215 (2020).
27. Niu, S. *et al.* Low Ru loading RuO₂/(Co,Mn)₃O₄ nanocomposite with modulated electronic structure for efficient oxygen evolution reaction in acid. *Appl. Catal. B* **297** (2021).
28. Li, N. *et al.* Identification of the active-layer structures for acidic oxygen evolution from 9R-BaIrO₃ electrocatalyst with enhanced iridium mass activity. *J. Am. Chem. Soc.* **143**, 18001–18009 (2021).
29. Nong, H. N. *et al.* A unique oxygen ligand environment facilitates water oxidation in hole-doped IrNiOx core–shell electrocatalysts. *Nat. Catal.* **1**, 841–851 (2018).
30. Li, L. *et al.* In situ/operando capturing unusual Ir⁶⁺ facilitating ultrafast electrocatalytic water oxidation. *Adv. Funct. Mater.* **31** (2021).
31. Meng, G. *et al.* Strain regulation to optimize the acidic water oxidation performance of atomic-layer IrOx. *Adv. Mater.* **31**, 1903616 (2019).

32. Suntivich, J., May, K. J., Gasteiger, H. A., Goodenough, J. B. & Shao-Horn, Y. A perovskite oxide optimized for oxygen evolution catalysis from molecular orbital principles. *Science* **334**, 1383–1385 (2011).
33. Huang, J. *et al.* Modifying redox properties and local bonding of Co_3O_4 by CeO_2 enhances oxygen evolution catalysis in acid. *Nat. Commun.* **12**, 3036 (2021).
34. Harada, M., Kotegawa, F. & Kuwa, M. Structural changes of spinel MCo_2O_4 (M = Mn, Fe, Co, Ni, and Zn) electrocatalysts during the oxygen evolution reaction investigated by in situ X-ray absorption spectroscopy. *ACS Appl. Energy Mater.* **5**, 278–294 (2022).
35. Li, L. *et al.* Compensating electronic effect enables fast site-to-site electron transfer over ultrathin RuMn nanosheet branches toward highly electroactive and stable water splitting. *Adv. Mater.*, 2105308 (2021).
36. Mesa, C. A. *et al.* Multihole water oxidation catalysis on haematite photoanodes revealed by operando spectroelectrochemistry and DFT. *Nat. Chem.* **12**, 82–89 (2020).
37. Zaman, W. Q. *et al.* Ni – Co codoping breaks the limitation of single-metal-doped IrO_2 with higher oxygen evolution reaction performance and less iridium. *ACS Energy Lett.* **2**, 2786–2793 (2017).
38. Zhang, J. *et al.* Iridium nanoparticles anchored on 3D graphite foam as a bifunctional electrocatalyst for excellent overall water splitting in acidic solution. *Nano Energy* **40**, 27–33 (2017).
39. Jin, Z. *et al.* Nanoporous Al-Ni-Co-Ir-Mo high-entropy alloy for record-high water splitting activity in acidic Environments. *Small* **15**, 1904180 (2019).
40. Lv, F. *et al.* Ir-based alloy nanoflowers with optimized hydrogen binding energy as bifunctional electrocatalysts for overall water splitting. *Small Methods* **4**, 1900129 (2019).
41. You, H. *et al.* Highly active and stable water splitting in acidic media using a bifunctional iridium/cucurbit[6]uril catalyist. *ACS Energy Lett.* **4**, 1301–1307 (2019).
42. Liu, N. *et al.* Hierarchically porous nickel–iridium–ruthenium–aluminum alloys with tunable compositions and electrocatalytic activities towards the oxygen/hydrogen evolution reaction in acid electrolyte. *J. Mater. Chem. A* **8**, 6245–6255 (2020).
43. Wang, H. *et al.* Significantly enhanced overall water splitting performance by partial oxidation of Ir through Au modification in core-shell alloy structure. *J. Am. Chem. Soc.* **143**, 4639–4645 (2021).
44. Navarro-Flores, E., Chong, Z. & Omanovic, S. Characterization of Ni, NiMo, NiW and NiFe electroactive coatings as electrocatalysts for hydrogen evolution in an acidic medium. *J. Mol. Catal. A Chem.* **226**, 179–197 (2005).
45. Ito, Y. *et al.* Cooperation between holey graphene and NiMo alloy for hydrogen evolution in an acidic electrolyte. *ACS Catal.* **8**, 3579–3586 (2018).
46. McCrory, C. C., Jung, S., Peters, J. C. & Jaramillo, T. F. Benchmarking heterogeneous electrocatalysts for the oxygen evolution reaction. *J. Am. Chem. Soc.* **135**, 16977–16987 (2013).

Figures

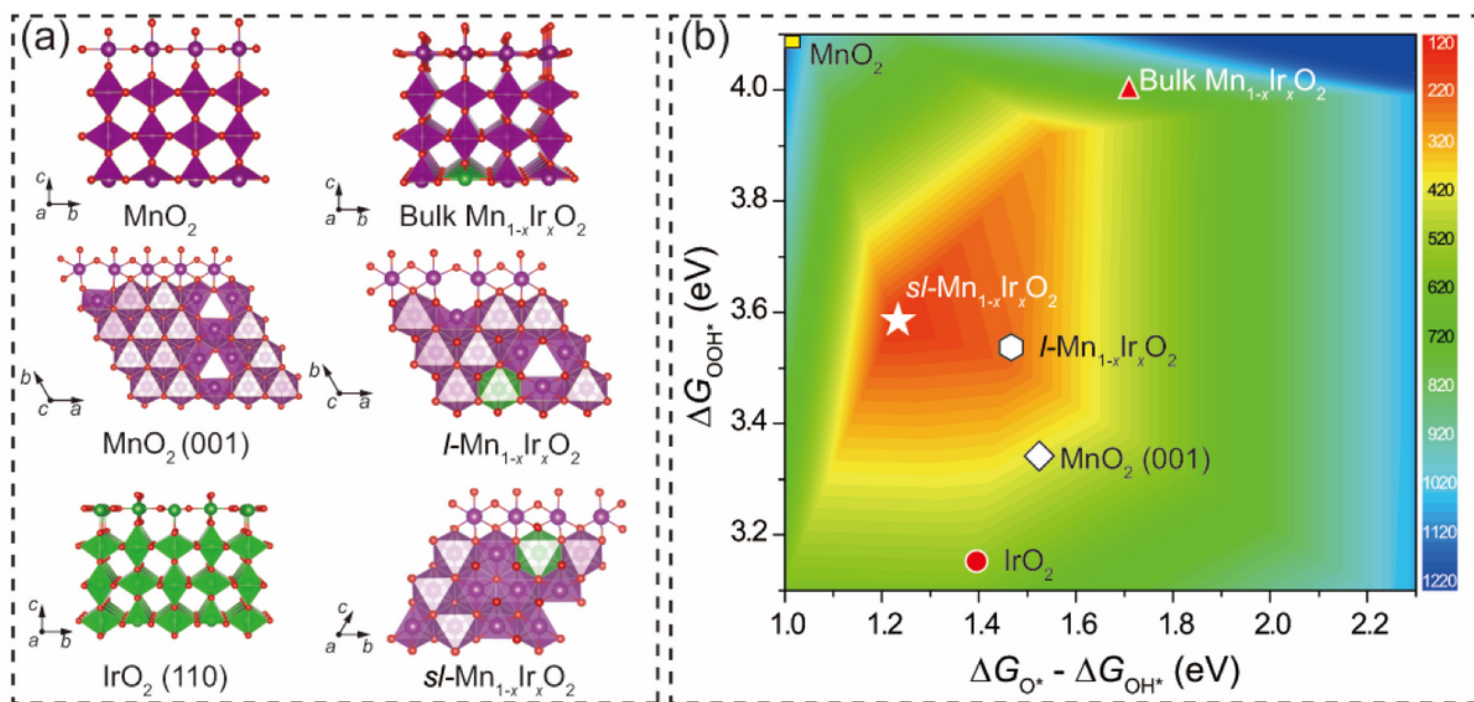


Figure 1

(a) Calculated structural modules of bulk MnO₂, layered *d*-MnO₂ (MnO₂ (001)), IrO₂, bulk Mn_{1-x}Ir_xO₂, *l*-Mn_{1-x}Ir_xO₂ and *s/l*-Mn_{1-x}Ir_xO₂. **(b)** Contour plot of theoretical overpotential as function of $\Delta G_{O^*} - \Delta G_{OH^*}$ and ΔG_{OOH^*} . The corresponding overpotentials (mV) are shown in the right bar of **(b)**. The crystal structure in **(a)** are shown in both ball-stick models (the first atomic layer) and polyhedral models (the bottom layers).

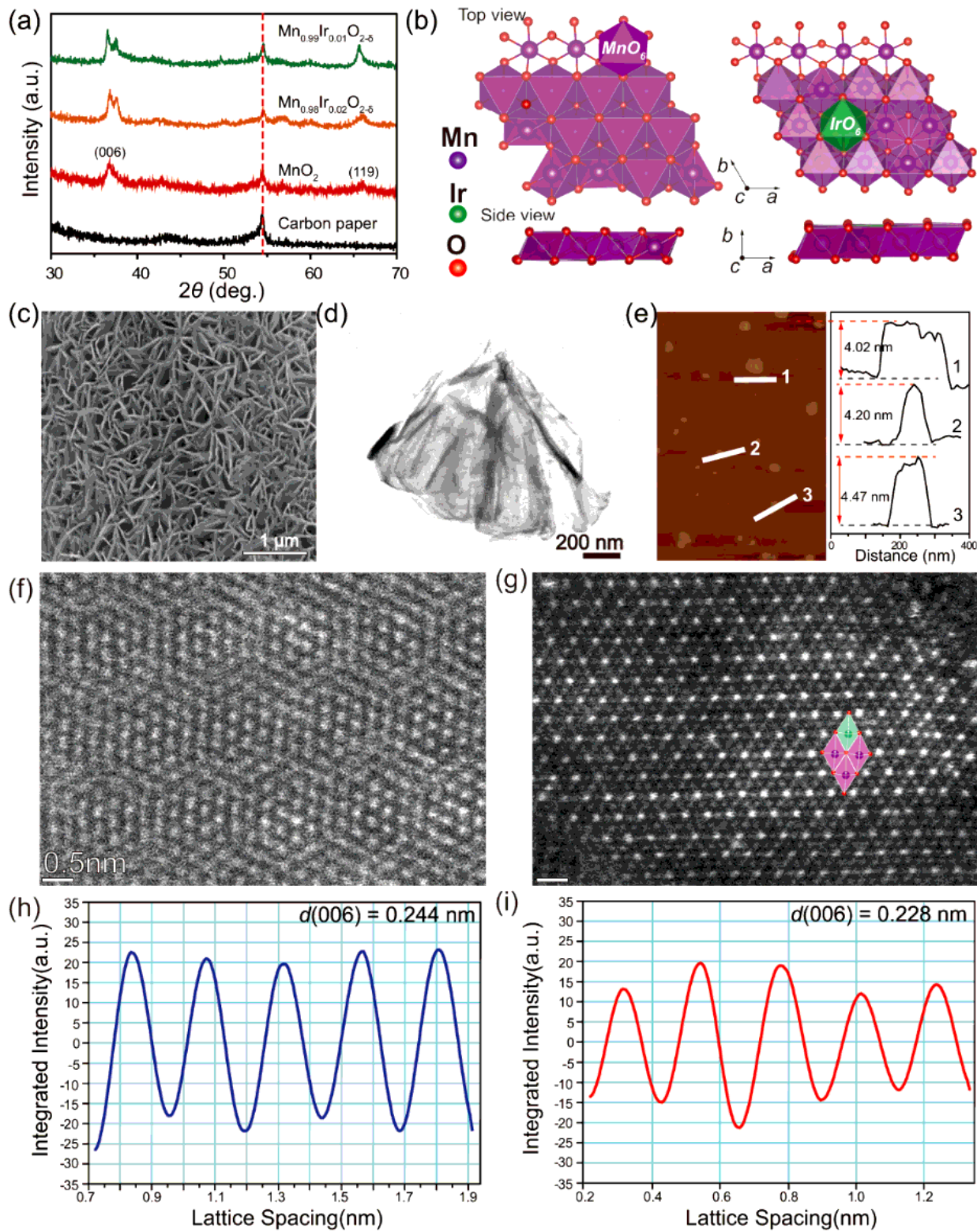


Figure 2

(a) XRD patterns of carbon paper substrate, $d\text{-MnO}_2$ and $s\text{-Mn}_{1-x}\text{Ir}_x\text{O}_2$. (b) crystal structure. (Left image: crystal structure of $d\text{-MnO}_2$; right image: crystal structure of $s\text{-Mn}_{1-x}\text{Ir}_x\text{O}_2$.) (c) SEM of $s\text{-Mn}_{0.98}\text{Ir}_{0.02}\text{O}_2$. (d) TEM image of $s\text{-Mn}_{0.98}\text{Ir}_{0.02}\text{O}_2$. (e) AFM of $s\text{-Mn}_{0.98}\text{Ir}_{0.02}\text{O}_2$. Height profiles of AFM image is shown in right plot of (e). (f) HAADF-STEM image of $s\text{-Mn}_{0.98}\text{Ir}_{0.02}\text{O}_2$. (g) HAADF-STEM image of $s\text{-}$

$\text{Mn}_{0.98}\text{Ir}_{0.02}\text{O}_2$. **(h)** The strength of lattice spacing in $\text{Mn}_{0.98}\text{Ir}_{0.02}\text{O}_2$. **(i)** The strength of lattice spacing in $s/\text{Mn}_{0.98}\text{Ir}_{0.02}\text{O}_2$. Scale bars in **(f and g)** are 0.5 nm.

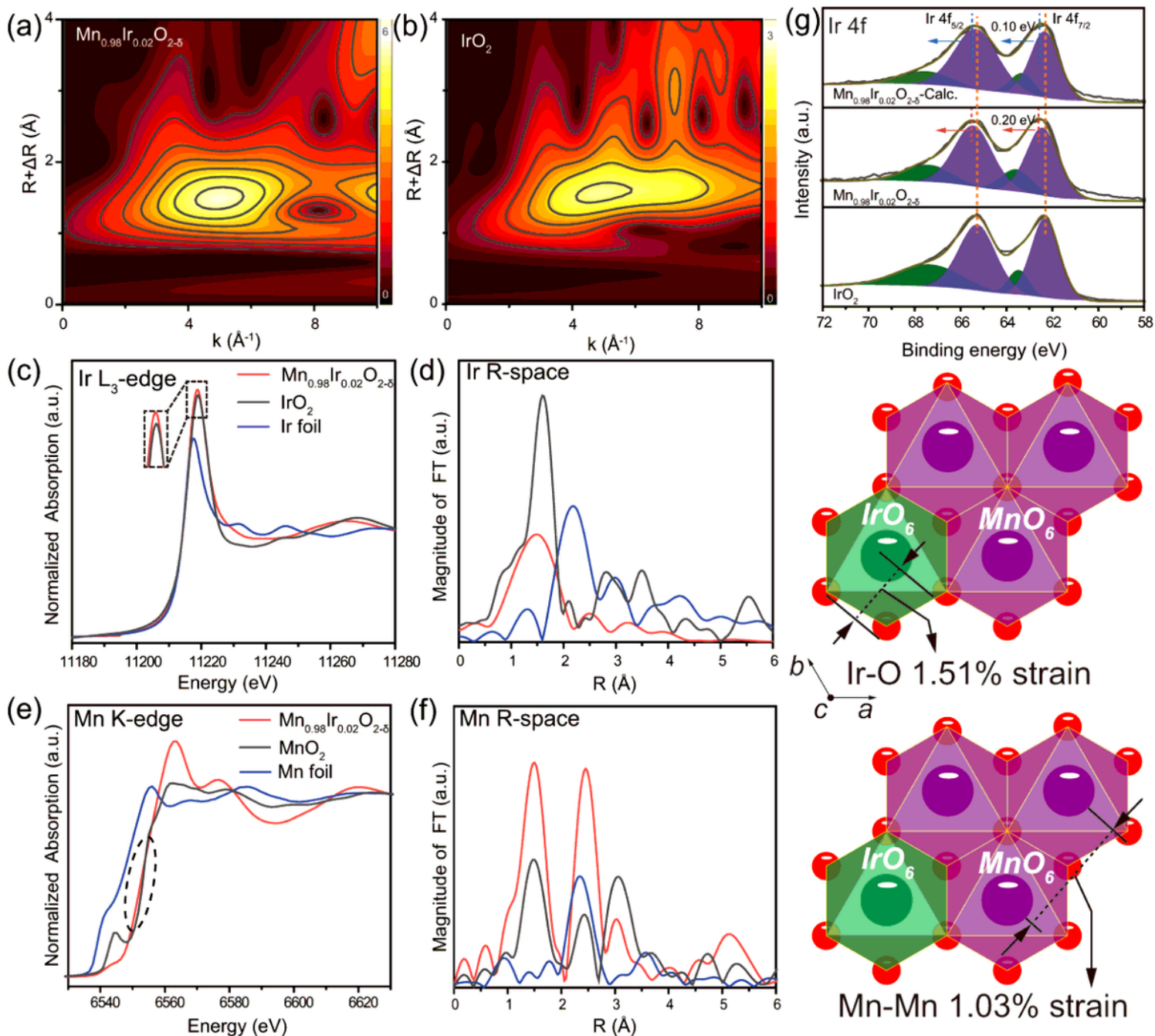


Figure 3

(a) Wavelet transform for $s/\text{Mn}_{0.98}\text{Ir}_{0.02}\text{O}_2$. **(b)** Wavelet transform for IrO_2 . **(c)** XAFS spectra of the Ir L₃-edge. **(d)** FT-EXAFS spectra of the Ir L₃-edge. **(e)** XAFS spectra of the Mn K-edge. **(f)** FT-EXAFS spectra of the Mn K-edge. **(g)** Ir 4f XPS. The images beside **(d)** and **(f)** are the schematic illustrations of the measured lattice compressive strains from the results of **(a)** to **(f)**, respectively. Ir-O bond has 1.51% compressive strain, while Mn-Mn has 1.03% compressive strain.

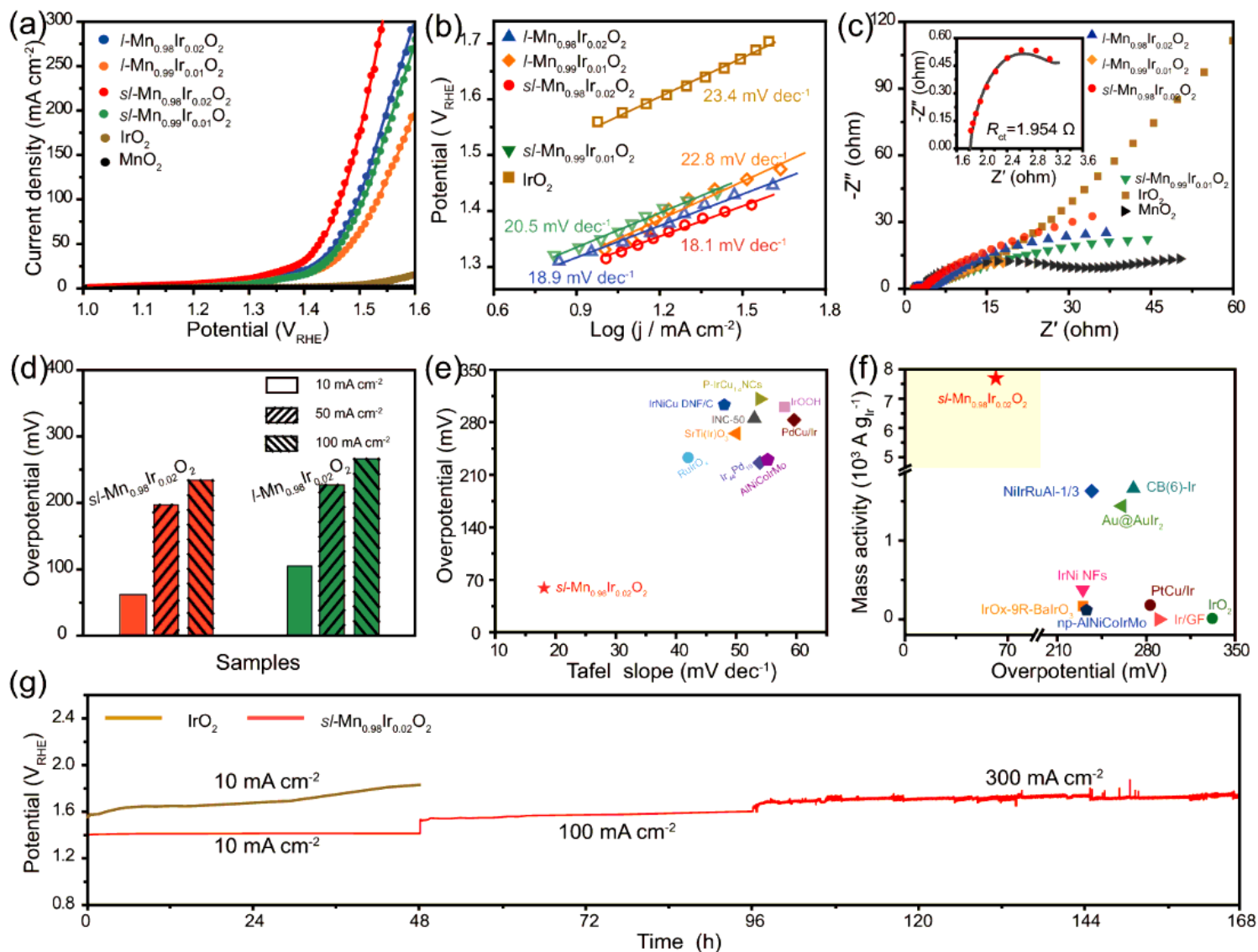


Figure 4

(a) OER polarization curves. (b) Corresponding Tafel slopes. (c) EIS curves (inset: the fitting result for $s\text{-Mn}_{0.98}\text{Ir}_{0.02}\text{O}_2$). (d) The overpotentials histograms at 10, 50 and 100 mA cm^{-2} , respectively. (e) Comparison of overpotential at 10 mA cm^{-2} and Tafel slope for $s\text{-Mn}_{0.98}\text{Ir}_{0.02}\text{O}_2$ with reported OER catalysts in acid media. (f) Comparison of mass activity in 270 mV and overpotential at 10 mA cm^{-2} with the-state-of-the-art Ir-contained electrocatalysts. (g) Chronopotentiometric stability test of $s\text{-Mn}_{0.98}\text{Ir}_{0.02}\text{O}_2$ at 10, 100 and 300 mA cm^{-2} , and IrO_2 was tested at 10 mA cm^{-2} for comparison.

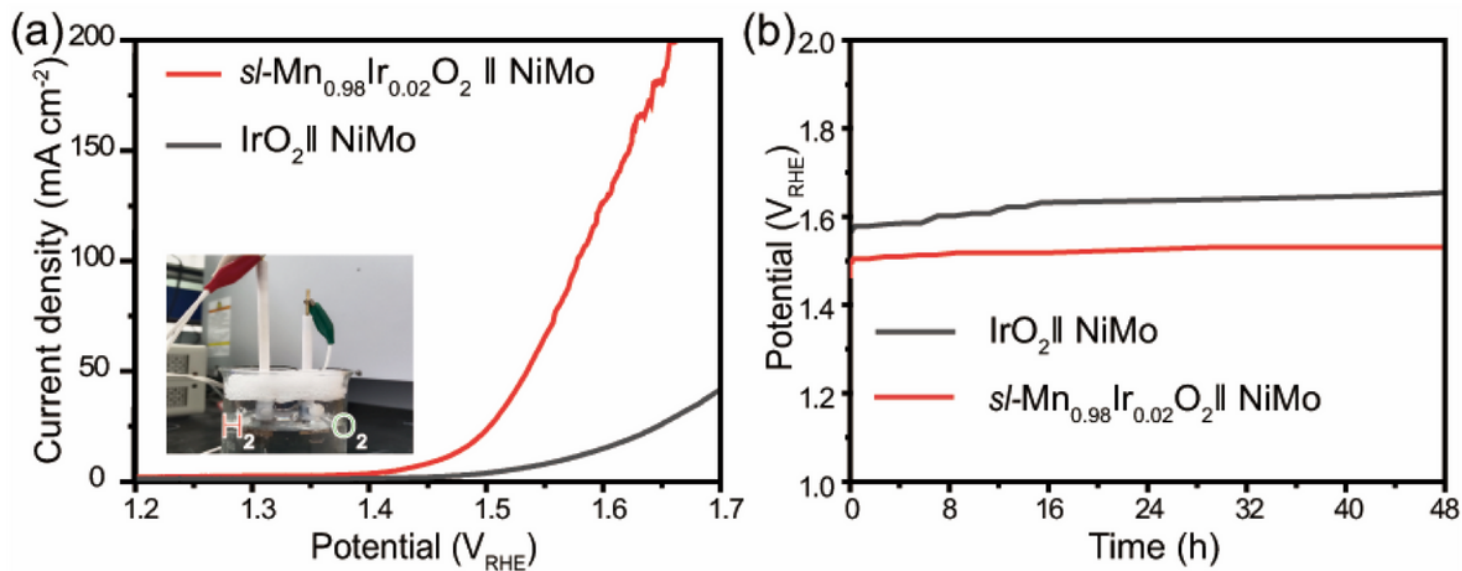


Figure 5

(a) Polarization curves of *s*-Mn_{0.98}Ir_{0.02}O₂ // NiMo and IrO₂ // NiMo two-electrode overall water splitting systems in 0.5 M H₂SO₄ (commercial NiMo alloys as a cathode). **(b)** Chronopotentiometric stability tests for two-electrode overall water splitting systems at 10 mA cm⁻².

Supplementary Files

This is a list of supplementary files associated with this preprint. Click to download.

- [SupportingInformation030211.docx](#)